Applied Physics Letters ARTICLE pubs.aip.org/aip/apl

# Ionically driven synthesis and exchange bias in $Mn_4N/MnN_x$ heterostructures

Cite as: Appl. Phys. Lett. **123**, 082403 (2023); doi: 10.1063/5.0165895
Submitted: 1 July 2023 · Accepted: 9 August 2023 ·
Published Online: 22 August 2023



Zhijie Chen,[1] Christopher J. Jensen,[1] Chen Liu,[2] Xixiang Zhang,[2] and Kai Liu[1,a)]

## AFFILIATIONS

[1]Physics Department, Georgetown University, Washington, District of Columbia 20057, USA
[2]King Abdullah University of Science & Technology, Thuwal 23955-6900, Saudi Arabia

**Note:** This paper is part of the APL Special Collection on Ferrimagnetic Spintronics.
[a)]**Author to whom correspondence should be addressed:** kai.liu@georgetown.edu

## ABSTRACT

Ferrimagnets have received renewed attention as a promising platform for spintronic applications. Of particular interest is the $Mn_4N$ from the $\varepsilon$-phase of the manganese nitride as an emergent rare-earth-free spintronic material due to its perpendicular magnetic anisotropy, small saturation magnetization, high thermal stability, and large domain wall velocity. We have achieved high-quality (001)-ordered $Mn_4N$ thin film by sputtering Mn onto $\eta$-phase $Mn_3N_2$ seed layers on Si substrates. As the deposited Mn thickness varies, nitrogen ion migration across the $Mn_3N_2$/Mn layers leads to a continuous evolution of the layers to $Mn_3N_2/Mn_2N/Mn_4N$, $Mn_2N/Mn_4N$, and eventually $Mn_4N$ alone. The ferrimagnetic $Mn_4N$, indeed, exhibits perpendicular magnetic anisotropy and forms via a nucleation-and-growth mechanism. The nitrogen ion migration is also manifested in a significant exchange bias, up to 0.3 T at 5 K, due to the interactions between ferrimagnetic $Mn_4N$ and antiferromagnetic $Mn_3N_2$ and $Mn_2N$. These results demonstrate a promising all-nitride magneto-ionic platform with remarkable tunability for device applications.





Ferrimagnets (FiMs) are characterized by antiparallel-coupled magnetic sublattices with different magnetic moments. They have gained tremendous interest recently as a promising platform for spintronic applications as they offer the combined benefits of ferromagnets (FMs) and antiferromagnets (AFs),[1–4] such as easy manipulation with an external magnetic field and fast spin dynamics.[5] Moreover, some FiMs such as rare-earth iron garnets,[6] rare-earth-transition metal films,[1] and $Mn_4N$[7] also possess perpendicular magnetic anisotropy (PMA) under appropriate growth conditions, a desirable functionality for device applications. Among them, $Mn_4N$ stands out due to its high Curie temperature ($T_C = 745$ K),[8] PMA,[7,9–11] small saturation magnetization (up to 145 emu/cm$^3$),[9] large domain wall velocity,[12] and possibility of hosting non-trivial spin textures.[13,14] It can also be doped with other elements to change its magnetic properties and compensation point.[15–17] As the only ferrimagnetic phase among the four stable manganese nitrides,[18] namely, $\theta$-MnN,[19] $\eta$-$Mn_3N_2$,[20,21] $\zeta$-$Mn_2N$,[22] and $\varepsilon$-$Mn_4N$,[8] $Mn_4N$ has an anti-perovskite structure with two inequivalent and anti-aligned Mn sublattices at the corners and face centers, and a nitrogen atom at the body center.

Furthermore, there have been emerging interests in magneto-ionics, where energy-efficient control of magnetic properties can be achieved via ionic migration.[23–40] Nitrogen-based magneto-ionics has been shown to exhibit good cyclabilities and fast ionic migration.[34,41–43] Recently, nitride-based exchange bias has been reported in MnN/CoFe heterostructures, which can be manipulated via nitrogen ion migration in and out of the MnN layer using an electric field.[44] This motivates us to build an all-nitride magneto-ionic system taking advantage of the different magnetic phases in Mn nitrides.

$Mn_4N$ thin films are typically grown onto $SrTiO_3$ or MgO substrates at elevated temperatures through molecular beam epitaxy, pulsed laser deposition, or reactive sputtering in a nitrogen environment.[7,9–12,14] The film quality is susceptible to the nitrogen flow rate or partial pressure, and the optimum growth conditions vary from study to study.[7,11] It is challenging to grow high-quality thin films of $Mn_4N$ directly on Si substrates,[45,46] which are CMOS compatible. In this work, we demonstrate that high-quality (001)-ordered $Mn_4N$ thin films can be grown on Si substrates by directly sputtering pure Mn onto an $Mn_3N_2$ seed layer at elevated temperatures, resulted from the chemical reaction between Mn and the nitrogen in the $Mn_3N_2$ seed layer. In a nominally $Mn_3N_2$ (20 nm)/Mn ($t_{Mn}$) series of samples, by changing the deposited Mn thickness $t_{Mn}$ from 0 to 50 nm, nitrogen ion migration gradually transforms the layers into $Mn_3N_2/Mn_2N/Mn_4N$,

$Mn_2N/Mn_4N$, and eventually $Mn_4N$, confirmed by x-ray diffraction (XRD), transmission electron microscopy (TEM), and electron energy loss spectroscopy (EELS). The $Mn_4N$ films are found to exhibit PMA. First-order reversal curve (FORC) measurements reveal that the $Mn_4N$ forms with a nucleation-and-growth process. The nitrogen ion migration is also manifested in a significant exchange bias, up to 0.3 T at 5 K, due to the interaction between ferrimagnetic $Mn_4N$ and antiferromagnetic $Mn_3N_2$ and $Mn_2N$.

Seed layers of 20 nm $Mn_3N_2$ were first reactive-sputtered onto Si substrate with 285 nm thermally oxidized $SiO_2$ layer from an Mn target using direct current (dc) in an ultrahigh vacuum chamber with a base pressure better than $5 \times 10^{-8}$ Torr. The substrate temperature was kept at 450 °C, and the Ar:$N_2$ ratio was held at 1:1 with a 5 mTorr sputtering gas pressure. These $Mn_3N_2$ films were then left in vacuum for 30 min at the same substrate temperature to promote nitrogen reordering. Subsequently, 0–50 nm of Mn was deposited onto the $Mn_3N_2$ layer at the same 450 °C substrate temperature in an Ar-only environment. After deposition, substrate heating was immediately turned off, and the samples were cooled to room temperature before depositing a 5 nm Ti capping layer.

Structural characterizations were performed using XRD on a Panalytical X'Pert$^3$ MRD with symmetric $2\theta$–$\omega$ and grazing incidence geometries. Sample microstructures and composition analysis were done using an FEI Titan Themes Cubed G2 300 (Cs Probe) TEM at KAUST.

Magnetic measurements were carried out using a Quantum Design superconducting quantum interference device (SQUID) magnetometer MPMS3. Exchange bias was measured at 5 K by first field-cooling the sample from 300 K in a 2 T magnetic field, all in the out-of-plane (OP) geometry. FORC measurements[47–51] were done in a vibrating sample magnetometer at room temperature by saturating samples in a 1.5 T OP magnetic field and then measuring from a reversal field ($H_R$) back to saturation. This process was repeated at different $H_R$ to fill the interior of the hysteresis loop, creating a family of FORCs. A FORC distribution was then calculated using the following equation:

$$\rho(H, H_R) \equiv -\frac{1}{2M_S}\frac{\partial^2 M(H, H_R)}{\partial H\, \partial H_R}, \tag{1}$$

where $M_S$ is the saturation magnetization and $M(H, H_R)$ is the magnetization at the applied field $H$ with reversal field $H_R$. The FORC distribution can also be represented in terms of local coercive field and bias field ($H_C$, $H_B$) defined by $H_C = \frac{1}{2}(H - H_R)$ and $H_B = \frac{1}{2}(H + H_R)$.

The $\eta$-phase $Mn_3N_2$ is chosen as the seed layer for $Mn_4N$ growth because it provides the crystalline texture and nitrogen needed for the $Mn_4N$ growth.[52] As shown in Figs. 1(a) and 1(b), $Mn_3N_2$ is antiferromagnetic ($T_N \sim 925$ K), and its $c$-axis is about three times that of $Mn_4N$.[21,53] XRD reveals the growth of the $Mn_3N_2$ phase, shown in Fig. 1(c), with a preferred orientation along the (010) direction and the $c$-axis in the film plane. Furthermore, grazing incidence XRD confirms that all peaks are from $Mn_3N_2$ (supplementary material, Fig. S1). Upon depositing 40 nm of Mn, XRD shows that the film is primarily the $Mn_4N$ phase oriented along (001), with no appreciable $Mn_3N_2$ phase left, as shown in Fig. 1(d) and supplementary material, Fig. S1. Along with the structure changes, there is also a drastic change in the film magnetic properties. As shown in Fig. 1(e), the initial $Mn_3N_2$ layer does not exhibit any appreciable magnetic signal, consistent with its antiferromagnetic nature; interestingly, the sample deposited with Mn exhibits a square loop with a large coercivity (0.27 T) and a small $M_S$ (85 emu/cm$^3$) that are typical of $Mn_4N$ films.[7,9,10]

To understand how the film transforms from $Mn_3N_2$ to $Mn_4N$ by only depositing Mn, we have investigated a series of samples starting with 20 nm $Mn_3N_2$ seed layer, but the deposited Mn nominal thickness varied from 0 to 50 nm with a 5 nm step size. From now on, each sample is referred by its deposited Mn thickness ($t_{Mn}$) unless otherwise stated. Figure 2(a) reveals how the Mn nitride phase evolves across the samples. Starting from $t_{Mn} = 0$ nm, which is the $Mn_3N_2$ layer, the only peak is the $Mn_3N_2$ (020). As $t_{Mn}$ increases, a prominent peak emerges around 47.2°, corresponding to the $Mn_4N$ (002), indicating $Mn_4N$ formation as Mn is deposited. On the other hand, the $Mn_3N_2$ (020) peak diminishes and shifts to higher angles before eventually vanishing in the $t_{Mn} = 30$ nm sample. This trend indicates that the $Mn_3N_2$ phase is fading and is not as stable as $Mn_4N$ at high temperatures, consistent with prior studies.[19,54] Interestingly, as the $Mn_3N_2$ peak gets smaller, another peak emerges near 42.2° in the

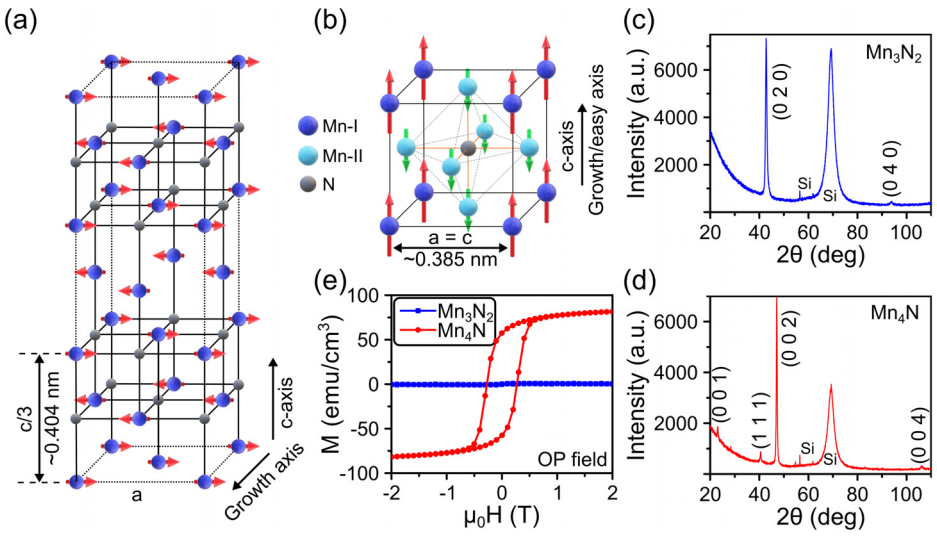


**FIG. 1.** Schematics showing the lattice structure and spin orientation of (a) $Mn_3N_2$ and (b) $Mn_4N$. XRD $2\theta$-$\omega$ scans of (c) 20 nm $Mn_3N_2$ seed layer and (d) $Mn_4N$ sample fabricated by depositing 40 nm Mn on top of 20 nm $Mn_3N_2$. (e) Room temperature out-of-plane hysteresis loops for the same $Mn_3N_2$ and $Mn_4N$ samples.

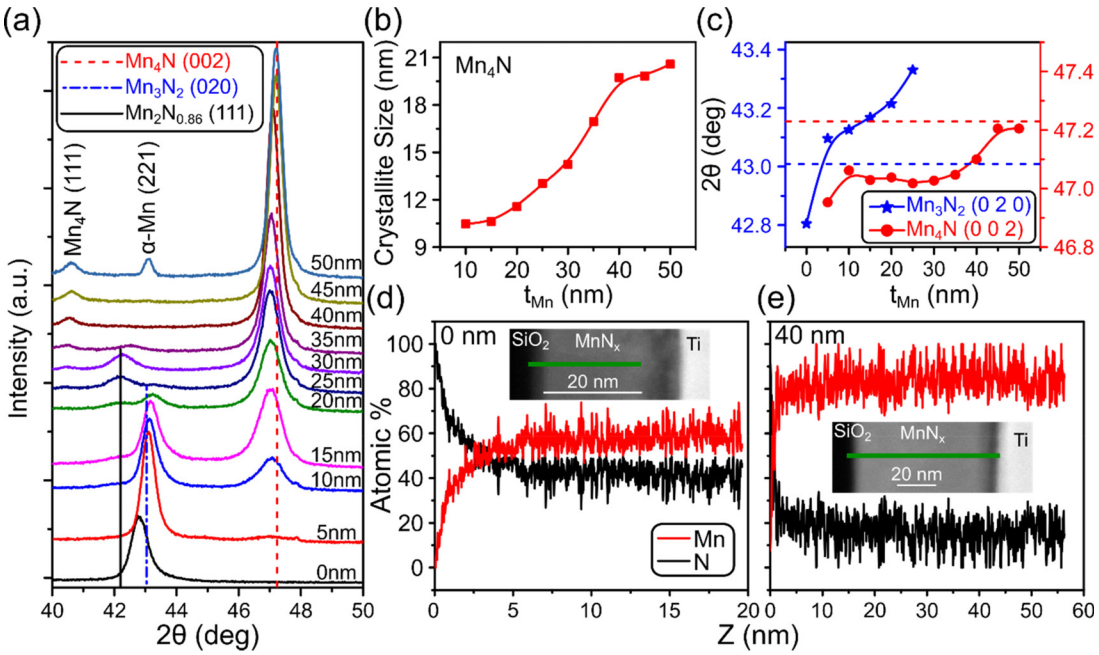


**FIG. 2.** (a) XRD $2\theta$-$\omega$ scans for nominally $Mn_3N_2$ (20 nm)/Mn ($t_{Mn}$) films, and $t_{Mn}$ is the deposited Mn thickness listed next to each curve. Vertical lines show the expected peak locations of $Mn_4N$ (002) (red), $Mn_3N_2$ (020) (blue), and $Mn_2N_{0.86}$ (111) (black). Trends showing (b) $Mn_4N$ crystallite size and (c) $Mn_4N$ (002) (red) and $Mn_3N_2$ (020) (blue) peak location variations. Solid lines are guides to the eye. Dotted horizontal lines are the expected peak locations for $Mn_4N$ (002) (red) and $Mn_3N_2$ (020) (blue). EELS scans along the green line in the TEM insets showing Mn:N ratio across the sample for (d) $t_{Mn} = 0$ nm and (e) $t_{Mn} = 40$ nm, where $Z = 0$ is the starting point of the interface between the substrate and $MnN_x$ layers.

$t_{Mn} = 20$ nm sample and grows larger before disappearing in the $t_{Mn} = 40$ nm sample. This peak is the (111) diffraction from the $\zeta$-phase $Mn_2N_{0.86}$, which has a thermal stability and nitrogen content between $\eta$-$Mn_3N_2$ and $\varepsilon$-$Mn_4N$.[18,19,54] In the $t_{Mn} = 40$ and 45 nm samples, both $Mn_3N_2$ and $Mn_2N$ peaks have vanished, while the $Mn_4N$ (002) peak gets even larger and closer to its expected location. Eventually, when $t_{Mn}$ reaches 50 nm, the $\alpha$-Mn (221) peak shows up near 43°, indicating that some deposited Mn remains unreacted as the entire nitride film is now $Mn_4N$. Grazing incidence scans are included in supplementary material, Fig. S1, consistent with Fig. 2(a), along with full range $2\theta$–$\omega$ scans (Fig. S2).

The $Mn_4N$ crystallite size has been estimated from the full-width-at-half-maximum (FWHM) of the (002) peak, after instrument broadening correction, using the Scherrer equation.[55] The $Mn_4N$ crystallite size nearly doubles as more Mn is deposited, reaching a plateau after $t_{Mn} = 40$ nm, as shown in Fig. 2(b). This is consistent with the trend in Fig. 2(a), where the $Mn_4N$ peak becomes sharper and more prominent, and $Mn_4N$ is the only phase after $t_{Mn}$ reaches 40 nm. This crystallite size estimation is rather simplified, as it ignores peak width contribution from other factors such as inhomogeneities in $d$-spacing. As the film stoichiometry changes due to the nitrogen migration, any spread in N-content and the lattice parameters would lead to a broadening of the peak width. Interestingly, the overall narrowing trend of the $Mn_4N$ peak width with increasing $t_{Mn}$ suggests that the stoichiometry variation is suppressed at high $t_{Mn}$, which is consistent with the aforementioned observation of a single $Mn_4N$ phase when $t_{Mn}$ reaches 40 nm. Moreover, the peak locations shift to higher angles as $t_{Mn}$ increases, as shown in Fig. 2(c). Nitride phases' lattice constants are known to be very sensitive to nitrogen content,[18] as interstitial nitrogen usually causes the lattices to expand. As $Mn_3N_2$ loses nitrogen to the deposited Mn, its lattice contracts, causing the $Mn_3N_2$ peak to shift to a higher angle until this phase is gone. The $Mn_4N$ peak location, on the other hand, stays relatively constant before changing rapidly beyond $t_{Mn} = 40$ nm, likely caused by the nitrogen redistribution within the $Mn_4N$ phase once the nitrogen from $Mn_3N_2$ and $Mn_2N$ has been depleted. Thus, we postulate that as Mn is deposited onto the $Mn_3N_2$ layer at elevated temperatures, it reacts with the nitrogen coming from $Mn_3N_2$ and forms $Mn_4N$. While $Mn_3N_2$ loses nitrogen, it first turns into $Mn_2N$ and eventually becomes $Mn_4N$. These reactions are summarized in Eq. (2a), and they can be combined into one chemical reaction [Eq. (2b)] since they are multistep reactions,

$$2Mn_3N_2 \rightarrow 3Mn_2N + N; \quad 4Mn + N \rightarrow Mn_4N; \quad 2Mn_2N \rightarrow Mn_4N + N, \tag{2a}$$

$$5Mn + Mn_3N_2 \rightarrow 2Mn_4N. \tag{2b}$$

We also calculated the enthalpy of formation for the reaction shown in Eq. (2b) to be −110 kJ/mol using the standard enthalpy of formation for $Mn_4N$ and $Mn_3N_2$,[54] indicating that this reaction is thermodynamically favorable.

Cross-sectional TEM and EELS lines scans were performed to explore the microstructure and nitrogen content evolution as $t_{Mn}$ varies. Figure 2(d) shows the EELS line scan along the film thickness (green line in the inset) for $t_{Mn} = 0$ nm. The Mn:N composition ratio

is determined to be 58:42, consistent with the nominal atomic ratio of $Mn_3N_2$. As $t_{Mn}$ increases to 40 nm, the EELS scan shown in Fig. 2(e) illustrates that the Mn:N ratio is now 84:16, also consistent with the nominal atomic ratio of $Mn_4N$. Interestingly, most of the nitride layers appear homogenous with constant Mn:N ratio from both the cross-sectional TEM and EELS, indicating that nitrogen in the $Mn_3N_2$ seed layer has redistributed to maintain a constant nitrogen concentration within the Mn nitrides after the Mn is deposited. These results further corroborate our postulation that nitrogen moves from the $Mn_3N_2$ seed layer into the Mn layer to form more stable $Mn_4N$.

We then investigate the magnetic properties of this series of samples. Figure 3(a) shows the room temperature hysteresis loops with in-plane (IP) and out-of-plane (OP) magnetic fields. The OP loops get more square and broader as $t_{Mn}$ increases from 10 to 50 nm, while the IP loops stay relatively constant. These trends are further revealed by plotting the squareness, or ratio of remanence magnetization ($M_r$) over $M_S$, for each sample, Fig. 3(b). The OP and IP remanence are small and stay relatively constant for $t_{Mn} < 20$ nm, indicating the lack of a clear magnetic easy axis. For 20 nm $< t_{Mn} <$ 35 nm, a sharp jump in OP remanence is observed, along with a drop in IP remanence, indicating a clear easy axis has been established in the OP direction. At $t_{Mn} > 35$ nm, the easy axis remains OP, while IP remanence increases slightly but remains low.

We have also calculated the uniaxial magnetic anisotropy constant ($K_u$, see the supplementary material). As shown in Fig. 3(c), $K_u$ starts out to be negative for $t_{Mn} = 5$ nm and shows a clear switching from negative to positive, especially when $t_{Mn} > 20$ nm, further confirming the magnetic easy axis switching to OP as more $Mn_4N$ is formed. Note that $K_u$ exhibits the largest value (0.03 MJ/m$^3$), or the film has the largest PMA when 35 nm $< t_{Mn} <$ 45 nm. This is also consistent with the XRD result, which shows that $Mn_4N$ is the only phase

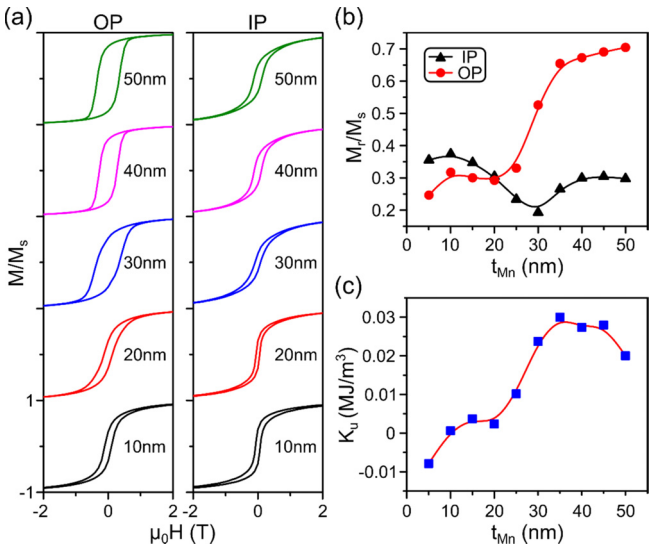


**FIG. 3.** (a) Room temperature hysteresis loop with out-of-plane (left) and in-plane (right) magnetic fields for nominally $Mn_3N_2$ (20 nm)/Mn ($t_{Mn}$) films, where $t_{Mn}$ is the deposited Mn thickness listed next to each curve. Trends for the (b) in-plane and out-of-plane remanence and (c) $K_u$ as $t_{Mn}$ increases. Solid lines in (b) and (c) are guides to the eye.

for this $t_{Mn}$ range. This $K_u$ value is smaller than other reported values, which range from 0.05 to 0.2 MJ/m$^3$.[7,9–11,56,57] The uniaxial anisotropy has been attributed to the tetragonal distortion caused by in-plane tensile strains.[7,9,10] However, in this study, the films that show the largest PMA has $c/a$ close to 1 (Table 1 in the supplementary material). The lack of in-plane strain may be the reason for our somewhat smaller $K_u$ values since the films are deposited onto an amorphous $SiO_2$ layer. Additionally, the sizeable PMA in our films may have come from other contributions such as the shape anisotropy of the $Mn_4N$ grains.[58]

To investigate how the $Mn_4N$ phase evolves with $t_{Mn}$ and the corresponding magnetization reversal, we have carried out FORC studies in the OP geometry at room temperature, as shown in Fig. 4. For the $t_{Mn} = 10$ and 20 nm samples, individual FORCs fill the major loops in a slanted fashion, Figs. 4(a) and 4(c), respectively. The corresponding FORC distributions exhibit a prominent vertical ridge centered around $H_C = 0$, which corresponds to reversible switching,[51,59] and a smaller horizontal feature centered at $\mu_0 H_C = 120$ and 150 mT [Figs. 4(b) and 4(d), respectively]. This indicates that the $Mn_4N$ film is mainly reversible and magnetically soft. Likely for this $t_{Mn}$ range, the $Mn_4N$ phase is just emerging in small clusters scattered in an antiferromagnetic matrix of $Mn_3N_2$ and $Mn_2N$. As more $Mn_4N$ is formed, families of FORCs for $t_{Mn} = 30$, 40, and 50 nm are considerably different, as individual FORCs return to positive saturation in a more horizontal fashion, consistent with the establishment of a magnetic easy axis [Figs. 4(e), 4(g), and 4(i)]. Their FORC distributions are also strikingly different. The previous large vertical reversible ridge at $\mu_0 H_C = 0$ becomes smaller and eventually vanishes in the $t_{Mn} = 50$ nm sample. The horizontal feature along the $H_C$ axis now becomes prominent and shifts to higher $\mu_0 H_C$ of 460, 310, and 390 mT [Figs. 4(f), 4(h), and 4(j), respectively]. The change in relative intensity of the horizontal and vertical FORC features likely indicates that $Mn_4N$ forms via a nucleation-and-growth mechanism, similar to that reported previously in the ordering of $L1_0$ FeCuPt.[59]

In this nominally $Mn_3N_2$ (20 nm)/Mn ($t_{Mn}$) series of samples, the evolution of the AF phase and the emergence of the FiM phase are also manifested in the exchange bias effect, which was studied at 5 K after cooling the samples from room temperature in a positive 2 T OP magnetic field. A significant horizontal shift to the negative field direction, up to 300 mT, and a coercivity enhancement can be seen, Fig. 5(a), typical of exchange bias systems.[44,60–62] The $t_{Mn}$ dependence of coercivity ($H_C$) and exchange field ($H_E$) both exhibit non-monotonic trends, with an intriguing peak around 20 nm $< t_{Mn} <$ 30 nm, as shown in Fig. 5(b). These trends are likely a combined effect from the AF phase evolution as well as the FiM thickness and $M_S$ variations. To further explore the exchange anisotropy independent of the FiM, we have evaluated the interfacial exchange energy ($J_{int}$) per unit area using the following equation:[60,62]

$$J_{int} = M_{FiM} t_{FiM} H_E = m_{FiM} H_E / A, \quad (3)$$

where $M_{FiM}$, $m_{FiM}$, and $t_{FiM}$ are the FiM saturation magnetization, saturation magnetic moment, and layer thickness, respectively, $H_E$ is the exchange field, and $A$ is the sample area. As shown in Fig. 5(c), the dependence of $J_{int}$ on $t_{Mn}$ exhibits a bell-shaped plot that peaks around 20–30 nm. $J_{int}$ is small and increases continuously for $t_{Mn}$ of 5–15 nm, where the dominating AF phase is $Mn_3N_2$, as observed by XRD. Due to the high $T_N$ of $Mn_3N_2$, only a small fraction of the AF spins is aligned to pin $Mn_4N$ by field-cooling from room temperature,

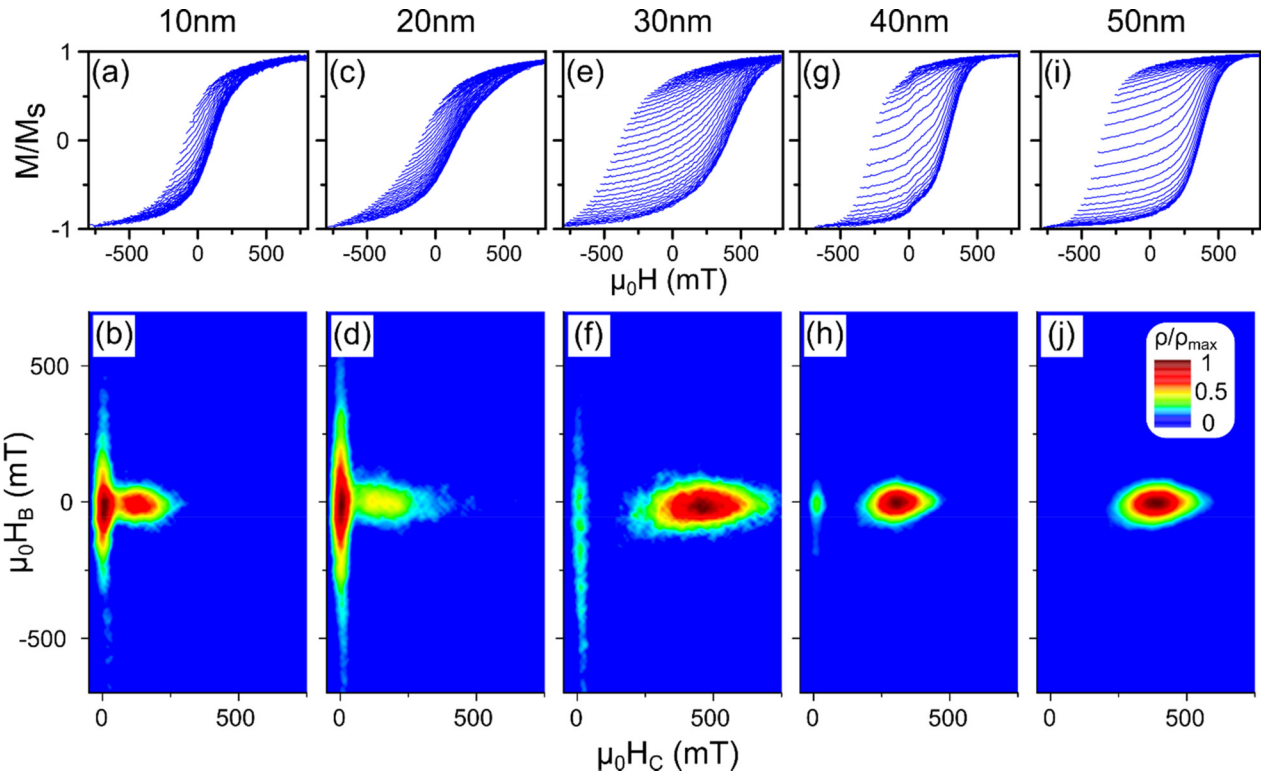


**FIG. 4.** Families of FORCs (top row) and FORC distributions (bottom row) for [(a) and (b)] $t_{Mn} = 10$ nm, [(c) and (d)] 20 nm, [(e) and (f)] 30 nm, [(g) and (h)] 40 nm, and [(i) and (j)] 50 nm. $t_{Mn}$ is the deposited Mn thickness on top of the 20 nm $Mn_3N_2$ seed layer.

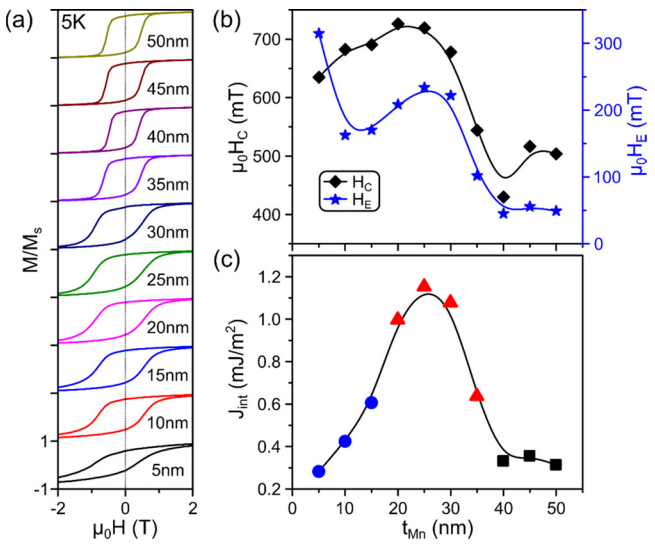


**FIG. 5.** (a) Hysteresis loops of the nominally $Mn_3N_2$ (20 nm)/Mn ($t_{Mn}$) series of samples measured at 5 K after 2 T field-cooling from 300 K, with the $t_{Mn}$ listed for each sample. (b) Dependence of coercivity (black) and exchange field (blue) on $t_{Mn}$ at 5 K. (c) Dependence of interfacial exchange energy on $t_{Mn}$ at 5 K where the color represents the different dominating antiferromagnetic phases: $Mn_3N_2$ (blue), $Mn_2N$ (red), and no antiferromagnets (black). Solid lines in (b) and (c) are guides to the eye.

resulting in a small $J_{int}$. However, for 20 nm $< t_{Mn} <$ 35 nm samples, another AF phase, $Mn_2N$, starts to dominate. By field-cooling from 300 K, the $Mn_2N$ is effectively coupled with $Mn_4N$, resulting in a significant exchange bias at 5 K. Exchange energy then quickly decreases as $Mn_2N$ is turned into $Mn_4N$. By $t_{Mn} = 40$ nm, no AF phases can be identified from XRD, and $J_{int}$ mostly vanishes.

In summary, we have achieved high-quality $Mn_4N$ films growth by depositing pure Mn onto an $Mn_3N_2$ seed layer. By varying the Mn thickness $t_{Mn}$, the Mn phases in the starting $Mn_3N_2$/Mn bilayers can be continuously tuned to be $Mn_3N_2$/$Mn_2N$/$Mn_4N$, $Mn_2N$/$Mn_4N$, and eventually to $Mn_4N$ alone, as observed by XRD and TEM/EELS. With increasing $t_{Mn}$, more $Mn_4N$ is formed, with an increasing PMA reaching 0.03 MJ/m$^3$. FORC measurements further reveal that $Mn_4N$ forms via a nucleation-and-growth mechanism. A large exchange bias up to 0.3 T is found at 5 K in this all-nitride system. The variation of the exchange anisotropy is further attributed to the phase change of the antiferromagnets caused by nitrogen redistribution. These results demonstrate an effective all-nitride magneto-ionic platform for studying the properties of the emergent ferrimagnetic $Mn_4N$ and its potential applications in spintronics.

See the supplementary material for grazing incidence and full range $2\theta$–$\omega$ x-ray diffraction patterns, Mn nitride phase evolution with layer thickness, cross-sectional TEM and EELS line scans, uniaxial magnetic anisotropy calculation, and additional sample information (PDF).

This work has been supported in part by the NSF (Nos. DMR-2005108 and ECCS-2151809), SMART (No. 2018-NE-2861), one of seven centers of nCORE, a Semiconductor Research Corporation program, sponsored by the National Institute of Standards and Technology (NIST), and by KAUST (No. OSR-2019-CRG8-4081). The acquisition of a Magnetic Property Measurements System (MPMS3), which was used in this investigation, was supported by the NSF-MRI program (No. DMR-1828420).

## AUTHOR DECLARATIONS

### Conflict of Interest

The authors have no conflicts to disclose.

### Author Contributions

**Zhijie Chen:** Conceptualization (equal); Data curation (lead); Formal analysis (lead); Investigation (lead); Methodology (equal); Validation (lead); Visualization (lead); Writing – original draft (lead); Writing – review & editing (equal). **Christopher J. Jensen:** Data curation (supporting); Formal analysis (supporting); Investigation (supporting); Methodology (equal); Validation (supporting); Writing – review & editing (equal). **Chen Liu:** Data curation (equal); Formal analysis (equal); Investigation (equal); Methodology (equal); Validation (equal); Visualization (equal); Writing – review & editing (equal). **Xixiang Zhang:** Formal analysis (supporting); Funding acquisition (equal); Investigation (equal); Methodology (equal); Project administration (equal); Resources (equal); Supervision (equal); Validation (equal); Writing – review & editing (equal). **Kai Liu:** Conceptualization (equal); Formal analysis (equal); Funding acquisition (equal); Investigation (equal); Methodology (equal); Project administration (equal); Resources (equal); Supervision (equal); Validation (equal); Visualization (equal); Writing – original draft (equal); Writing – review & editing (equal).

## DATA AVAILABILITY

The data that support the findings of this study are available within the article and its supplementary material.

## REFERENCES

[1]L. Caretta, M. Mann, F. Buttner, K. Ueda, B. Pfau, C. M. Gunther, P. Hessing, A. Churikova, C. Klose, M. Schneider, D. Engel, C. Marcus, D. Bono, K. Bagschik, S. Eisebitt, and G. S. D. Beach, Nat. Nanotechnol. **13**, 1154 (2018).
[2]R. Blasing, T. P. Ma, S. H. Yang, C. Garg, F. K. Dejene, A. T. N'Diaye, G. Chen, K. Liu, and S. S. P. Parkin, Nat. Commun. **9**, 4984 (2018).
[3]J. Finley and L. Liu, Appl. Phys. Lett. **116**, 110501 (2020).
[4]S. K. Kim, G. S. D. Beach, K.-J. Lee, T. Ono, T. Rasing, and H. Yang, Nat. Mater. **21**, 24 (2022).
[5]V. Baltz, A. Manchon, M. Tsoi, T. Moriyama, T. Ono, and Y. Tserkovnyak, Rev. Mod. Phys. **90**, 015005 (2018).
[6]C. O. Avci, A. Quindeau, C. F. Pai, M. Mann, L. Caretta, A. S. Tang, M. C. Onbasli, C. A. Ross, and G. S. Beach, Nat. Mater. **16**, 309 (2017).
[7]K. Kabara and M. Tsunoda, J. Appl. Phys. **117**, 17b512 (2015).
[8]W. J. Takei, R. R. Heikes, and G. Shirane, Phys. Rev. **125**, 1893 (1962).
[9]Y. Yasutomi, K. Ito, T. Sanai, K. Toko, and T. Suemasu, J. Appl. Phys. **115**, 17a935 (2014).
[10]T. Hirose, T. Komori, T. Gushi, A. Anzai, K. Toko, and T. Suemasu, AIP Adv. **10**, 025117 (2020).
[11]S. Isogami, K. Masuda, and Y. Miura, Phys. Rev. Mater. **4**, 014406 (2020).
[12]T. Gushi, M. Jovicevic Klug, J. Pena Garcia, S. Ghosh, J. P. Attane, H. Okuno, O. Fruchart, J. Vogel, T. Suemasu, S. Pizzini, and L. Vila, Nano Lett. **19**, 8716 (2019).
[13]T. Bayaraa, C. Xu, and L. Bellaiche, Phys. Rev. Lett. **127**, 217204 (2021).
[14]C. T. Ma, T. Q. Hartnett, W. Zhou, P. V. Balachandran, and S. J. Poon, Appl. Phys. Lett. **119**, 192406 (2021).
[15]K. Ito, Y. Yasutomi, S. Zhu, M. Nurmamat, M. Tahara, K. Toko, R. Akiyama, Y. Takeda, Y. Saitoh, T. Oguchi, A. Kimura, and T. Suemasu, Phys. Rev. B **101**, 104401 (2020).
[16]S. Ghosh, T. Komori, A. Hallal, J. Pena Garcia, T. Gushi, T. Hirose, H. Mitarai, H. Okuno, J. Vogel, M. Chshiev, J. P. Attane, L. Vila, T. Suemasu, and S. Pizzini, Nano Lett. **21**, 2580 (2021).
[17]S. Isogami, M. Ohtake, and Y. K. Takahashi, J. Appl. Phys. **131**, 073904 (2022).
[18]N. A. Gokcen, Bull. Alloy Phase Diagrams **11**, 33 (1990).
[19]K. Suzuki, T. Kaneko, H. Yoshida, Y. Obi, H. Fujimori, and H. Morita, J. Alloys Compd. **306**, 66 (2000).
[20]A. Leineweber, R. Niewa, H. Jacobs, and W. Kockelmann, J. Mater. Chem. **10**, 2827 (2000).
[21]H. Yang, H. Al-Brithen, A. R. Smith, J. A. Borchers, R. L. Cappelletti, and M. D. Vaudin, Appl. Phys. Lett. **78**, 3860 (2001).
[22]Y. Liu, L. Xu, X. Li, P. Hu, and S. Li, J. Appl. Phys. **107**, 103914 (2010).
[23]M. Weisheit, S. Fähler, A. Marty, Y. Souche, C. Poinsignon, and D. Givord, Science **315**, 349 (2007).
[24]U. Bauer, L. Yao, A. J. Tan, P. Agrawal, S. Emori, H. L. Tuller, S. van Dijken, and G. S. D. Beach, Nat. Mater. **14**, 174 (2015).
[25]C. Bi, Y. Liu, T. Newhouse-Illige, M. Xu, M. Rosales, J. W. Freeland, O. Mryasov, S. Zhang, S. G. E. Te Velthuis, and W. G. Wang, Phys. Rev. Lett. **113**, 267202 (2014).
[26]D. A. Gilbert, J. Olamit, R. K. Dumas, B. J. Kirby, A. J. Grutter, B. B. Maranville, E. Arenholz, J. A. Borchers, and K. Liu, Nat. Commun. **7**, 11050 (2016).
[27]D. A. Gilbert, A. J. Grutter, E. Arenholz, K. Liu, B. J. Kirby, J. A. Borchers, and B. B. Maranville, Nat. Commun. **7**, 12264 (2016).
[28]K. Duschek, D. Pohl, S. Fähler, K. Nielsch, and K. Leistner, APL Mater. **4**, 032301 (2016).
[29]J. Walter, H. Wang, B. Luo, C. D. Frisbie, and C. Leighton, ACS Nano **10**, 7799 (2016).
[30]A. Quintana, E. Menendez, M. O. Liedke, M. Butterling, A. Wagner, V. Sireus, P. Torruella, S. Estrade, F. Peiro, J. Dendooven, C. Detavernier, P. D. Murray, D. A. Gilbert, K. Liu, E. Pellicer, J. Nogues, and J. Sort, ACS Nano **12**, 10291 (2018).
[31]A. J. Tan, M. Huang, C. O. Avci, F. Büttner, M. Mann, W. Hu, C. Mazzoli, S. Wilkins, H. L. Tuller, and G. S. D. Beach, Nat. Mater. **18**, 35 (2019).
[32]L. Herrera Diez, Y. T. Liu, D. A. Gilbert, M. Belmeguenai, J. Vogel, S. Pizzini, E. Martinez, A. Lamperti, J. B. Mohammedi, A. Laborieux, Y. Roussigné, A. J. Grutter, E. Arenholtz, P. Quarterman, B. Maranville, S. Ono, M. S. E. Hadri, R. Tolley, E. E. Fullerton, L. Sanchez-Tejerina, A. Stashkevich, S. M. Chérif, A. D. Kent, D. Querlioz, J. Langer, B. Ocker, and D. Ravelosona, Phys. Rev. Appl. **12**, 034005 (2019).
[33]J. Zehner, R. Huhnstock, S. Oswald, U. Wolff, I. Soldatov, A. Ehresmann, K. Nielsch, D. Holzinger, and K. Leistner, Adv. Electron. Mater. **5**, 1900296 (2019).
[34]J. de Rojas, A. Quintana, A. Lopeandía, J. Salguero, B. Muñiz, F. Ibrahim, M. Chshiev, A. Nicolenco, M. O. Liedke, M. Butterling, A. Wagner, V. Sireus, L. Abad, C. J. Jensen, K. Liu, J. Nogués, and J. L. Costa-Krämer, Nat. Commun. **11**, 5871 (2020).
[35]G. Chen, A. Mascaraque, H. Jia, B. Zimmermann, M. Robertson, R. L. Conte, M. Hoffmann, M. A. González Barrio, H. Ding, R. Wiesendanger, E. G. Michel, S. Blügel, A. K. Schmid, and K. Liu, Sci. Adv. **6**, eaba4924 (2020).
[36]J. Walter, B. Voigt, E. Day-Roberts, K. Heltemes, R. M. Fernandes, T. Birol, and C. Leighton, Sci. Adv. **6**, eabb7721 (2020).
[37]G. Chen, M. Robertson, M. Hoffmann, C. Ophus, A. L. F. Cauduro, R. Lo Conte, H. F. Ding, R. Wiesendanger, S. Blügel, A. K. Schmid, and K. Liu, Phys. Rev. X **11**, 021015 (2021).
[38]Y. Guan, X. Zhou, F. Li, T. Ma, S.-H. Yang, and S. S. P. Parkin, Nat. Commun. **12**, 5002 (2021).

[39]Q. Wang, Y. Gu, C. Chen, F. Pan, and C. Song, J. Phys. Chem. Lett. **13**, 10065 (2022).
[40]G. Chen, C. Ophus, A. Quintana, H. Kwon, C. Won, H. Ding, Y. Wu, A. K. Schmid, and K. Liu, Nat. Commun. **13**, 1350 (2022).
[41]J. de Rojas, J. Salguero, F. Ibrahim, M. Chshiev, A. Quintana, A. Lopeandia, M. O. Liedke, M. Butterling, E. Hirschmann, A. Wagner, L. Abad, J. L. Costa-Kramer, E. Menendez, and J. Sort, ACS Appl. Mater. Interfaces **13**, 30826 (2021).
[42]J. de Rojas, A. Quintana, G. Rius, C. Stefani, N. Domingo, J. L. Costa-Krämer, E. Menéndez, and J. Sort, Appl. Phys. Lett. **120**, 070501 (2022).
[43]Z. Tan, S. Martins, M. Escobar, J. de Rojas, F. Ibrahim, M. Chshiev, A. Quintana, A. Lopeandia, J. L. Costa-Krämer, E. Menéndez, and J. Sort, ACS Appl. Mater. Interfaces **14**, 44581 (2022).
[44]C. J. Jensen, A. Quintana, P. Quarterman, A. J. Grutter, P. P. Balakrishnan, H. Zhang, A. V. Davydov, X. Zhang, and K. Liu, ACS Nano **17**, 6745 (2023).
[45]K. M. Ching, W. D. Chang, T. S. Chin, J. G. Duh, and H. C. Ku, J. Appl. Phys. **76**, 6582 (1994).
[46]S. Nakagawa and M. Naoe, J. Appl. Phys. **75**, 6568 (1994).
[47]C. R. Pike, A. P. Roberts, and K. L. Verosub, J. Appl. Phys. **85**, 6660 (1999).
[48]J. E. Davies, O. Hellwig, E. E. Fullerton, G. Denbeaux, J. B. Kortright, and K. Liu, Phys. Rev. B **70**, 224434 (2004).
[49]D. A. Gilbert, G. T. Zimanyi, R. K. Dumas, M. Winklhofer, A. Gomez, N. Eibagi, J. L. Vicent, and K. Liu, Sci. Rep. **4**, 4204 (2014).
[50]J. A. De Toro, M. Vasilakaki, S. S. Lee, M. S. Andersson, P. S. Normile, N. Yaacoub, P. Murray, E. H. Sánchez, P. Muñiz, D. Peddis, R. Mathieu, K. Liu, J. Geshev, K. N. Trohidou, and J. Nogués, Chem. Mater. **29**, 8258 (2017).
[51]E. C. Burks, D. A. Gilbert, P. D. Murray, C. Flores, T. E. Felter, S. Charnvanichborikarn, S. O. Kucheyev, J. D. Colvin, G. Yin, and K. Liu, Nano Lett. **21**, 716 (2021).
[52]W. Li, X. Xu, T. Gao, T. Harumoto, Y. Nakamura, and J. Shi, J. Phys. D **55**, 275004 (2022).
[53]M. Tabuchi, M. Takahashi, and F. Kanamaru, J. Alloys Compd. **210**, 143 (1994).
[54]R. Yu, X. Chong, Y. Jiang, R. Zhou, W. Yuan, and J. Feng, RSC Adv. **5**, 1620 (2015).
[55]A. L. Patterson, Phys. Rev. **56**, 978 (1939).
[56]X. Shen, A. Chikamatsu, K. Shigematsu, Y. Hirose, T. Fukumura, and T. Hasegawa, Appl. Phys. Lett. **105**, 072410 (2014).
[57]W. Zhou, C. T. Ma, T. Q. Hartnett, P. V. Balachandran, and S. J. Poon, AIP Adv. **11**, 015334 (2021).
[58]A. Foley, J. Corbett, A. Khan, A. L. Richard, D. C. Ingram, A. R. Smith, L. Zhao, J. C. Gallagher, and F. Yang, J. Magn. Magn. Mater. **439**, 236 (2017).
[59]D. A. Gilbert, J. W. Liao, L. W. Wang, J. W. Lau, T. J. Klemmer, J. U. Thiele, C. H. Lai, and K. Liu, APL Mater. **2**, 086106 (2014).
[60]J. Nogués and I. K. Schuller, J. Magn. Magn. Mater. **192**, 203 (1999).
[61]S. M. Zhou, K. Liu, and C. L. Chien, Phys. Rev. B **58**, R14717 (1998).
[62]R. L. Stamps, J. Phys. D **33**, R247 (2000).